Title: 3D-printing of resilient biogels for omnidirectional and exteroceptive soft actuators
Short title: 3D-printed, eco-friendly soft actuators

Authors:
A. Heiden,[1, 2]† D. Preninger,[1, 2]† L. Lehner,[1, 2] M. Baumgartner,[1, 2, 3] M. Drack,[1, 2] E. Woritzka,[1, 2] D. Schiller,[1, 2] R. Gerstmayr,[2, 3] F. Hartmann,[1, 2, 4*] M. Kaltenbrunner,[1, 2*]

Affiliations:

[1]Division of Soft Matter Physics, Institute of Experimental Physics, Johannes Kepler University Linz; Altenbergerstr. 69, Linz, Austria.

[2]Soft Materials Lab, Linz Institute of Technology, Johannes Kepler University Linz; Altenbergerstr. 69, Linz, Austria.

[3]Institute of Polymer Science, Johannes Kepler University Linz; Altenbergerstr. 69, Linz, Austria.

[4]Current affiliation: Soft Transducers Laboratory (LMTS), École Polytechnique Fédérale de Lausanne (EPFL), Rue de la Maladière 71B, Neuchâtel 2000, Switzerland.

*Corresponding author. Email: martin.kaltenbrunner@jku.at, f.hartmann@epfl.ch

†These authors contributed equally to this work

Abstract:

Soft robotics greatly benefits from nature as a source of inspiration, introducing new means of safe interaction between robotic appliances and living organisms. In contrast, the materials involved are often non-biodegradable or stem from non-renewable resources, contributing to an ever-growing environmental footprint. Furthermore, conventional manufacturing methods such as mold casting are not suitable for replicating or imitating the complexity of nature's creations. Consequently, the inclusion of sustainability concepts alongside the development of new fabrication procedures is required. We report a customized 3D-printing process based on fused deposition modeling, printing a fully biodegradable gelatin-based hydrogel (biogel) ink into dimensionally stable, complex objects. This process enables fast and cost-effective prototyping of resilient, soft robotic applications from gels that stretch to six times their original length, as well as an accessible recycling procedure with zero waste . We present printed pneumatic actuators performing omnidirectional movement at fast response times (less than a second), featuring integrated 3D-printed stretchable waveguides, capable of both proprio- and exteroception. These soft devices are endowed with dynamic real-time control capable of automated search and wipe routines to detect and remove obstacles. They can be reprinted several times or disposed of hazard-free at the end of their lifetime, potentially unlocking a sustainable future for soft robotics.

One-Sentence Summary: 3D-printing of biodegradable hydrogels for omnidirectional actuators with multifaceted sensing abilities.

Main Text:

INTRODUCTION

Embedding robotics into our daily life bears promise in creating new machine-assisted environments, supporting healthcare and rehabilitation, or augmenting haptic sensation for interaction in virtual realities(*1–3*). However, such dynamic environments typically require extensive control algorithms, sensors, and feedback loops to enable safe interaction with people, in addition to customizable designs to fit both user and application. Robots made from soft materials mitigate some of these challenges through their adaptive, soft structure(*4*). Yet, without any sensor feedback, soft robots still rely on the observation and intervention of an operator. New and rapidly changing technologies also contribute to increasing amounts of tech-waste, accumulating to as much as over 100,000 tons per day in 2019 (*5*). Soft robotics in particular needs to improve in terms of sustainability, due to the limited lifetime of soft materials or for applications where, for example, deployed robots cannot be retrieved. Thus sustainable soft actuators and sensors from renewable, biodegradable, and recyclable resources are required to avoid additional waste streams(*6*).

Recent demonstrations of biodegradable soft robots approach this materials challenge with synthesized polyesters(*7*), self-healing proteins(*8*), or gelatin-based hydrogels(*9*, *10*). Despite achieving the high stretchability and resilience required for pneumatically driven actuators, these robots are processed by conventional molding techniques that only yield objects of limited geometry and feature size. This constrains their applicability, as their locomotion is often reduced to a single predefined pattern and limited rudimentary sensing capabilities are implemented. Achieving more complex tasks requires advanced and more versatile fabrication strategies such as extrusion-based 3D-printing that enable unmoldable robot geometries with integrated sensor designs.

Gelatin is a versatile biopolymer, which allows melt-extrusion and, when methacrylated, photopolymerization based printing(*11*). Applications range from scaffolds for tissue engineering(*12–15*) to micro-robots(*16*) and smart optical fibers(*17*). However, commercially available bioplotters or direct laser writing systems are very cost-intensive and essentially only yield small scale (micro- to millimeter) objects with moderate stretchability(*16*, *18*). Rapid prototyping of soft robots has a high demand for low-cost 3D-printing of centimeter-sized, highly-stretchable actuators and sensors. Keeping the technology sustainable also requires efficient reuse of previously printed materials to spare resources and establish ecological recycling routes in addition to biodegradation (Fig. 1 A).

Herein we present sustainable material approaches, fabrication strategies, and design concepts for 3D-printed soft actuators with integrated sensor networks. We utilize a customized extrusion system to 3D-print resilient yet entirely degradable biogels in a fused deposition modeling (FDM) printing process with a minimal feature size of 0.6 mm and aspect ratios of more than 3 (height to width). The printed biogels are highly stretchable to more than 500% ultimate strain and are directly reused by reprinting them up to five times. In combination with the improved mechanical properties of the material, our fabrication strategy enables us to realize dexterous soft pneumatically driven actuators capable of omnidirectional motion with bending angles up to 74 degrees. Inspired by nature, where intricate sensor networks are essential for all forms of locomotion, we directly combine optical sensor networks based on stretchable waveguides with these soft robotic actuators. This combination enables integrated curvature, direction, and force sensing with high precision. By incorporating our 3D-printing technique to print the main actuator body and the waveguides, we minimized the production steps for this multifunctional device. We

demonstrated the robot's capabilities by implementing a search and wipe routine, utilizing its sensing features to detect and remove obstacles (Fig. 1 B). At the same time, the printed biogel can be easily reused or disposed of without environmental concerns since it is fully biodegradable(*10*) and dissolves in water within practical timescales (Fig. 1 C). Going beyond previously reported mold-casting of biogels, the here presented controlled printing process allows finer features and fabrication of multi-degree of freedom (DOF) actuators with soft sensors, while at the same time increasing the material's stretchability by about 140%. Mold-free fabrication and material re-usability in addition speed up prototyping and reduce waste generation.

RESULTS

3D-printing of biogel inks

Soft and highly stretchable materials are mandatory in the engineering processes of soft robotic applications. Despite their vast proliferation, silicone elastomers such as polydimethylsiloxane (PDMS) are non-biodegradable, require non-renewable resources and, once crosslinked, are no longer reshapeable or reusable. Addressing resource sustainability and waste reduction, elastic materials from biopolymers like gelatin(*9*, *19*), alginate(*20*, *21*) or cellulose(*22*, *23*) and synthetic polyesters such as poly(glycerol sebacate)(*24*) have emerged as promising candidates for biodegradable, renewable, and/or recyclable solutions across many application areas. However, these existing approaches either lack the mechanical stability, reusability or biodegradability necessary for completely sustainable and practical devices. In this work, we use previously reported resilient yet entirely degradable gelatin-based hydrogels(*10*). Their tunability (elastic modulus, 0.3-3 MPa) and high stretchability (> 300%) result from the introduction of glycerol and sugar syrup to the main gelatin network, whereas the addition of citric acid regulates the pH-value to prevent bacterial growth. This composition allows enzymatic degradation within a few days in sewage (see supplementary materials for details, Fig. S1), yet has a long shelf life and nearly unchanged mechanical properties for timescales beyond one year in ambient conditions.

For the extrusion of these biogels within a 3D-printing process, we used an existing paste extruder design(*25*) and adapted it to fit the needs of biogel printing. To this end, we integrated the extruder into a Makerbot 2X (© 2009–2021 MakerBot Industries) 3D-printer and implemented a two-stage heating system (Fig. 2 A) to control the temperature of the reservoir and at the extrusion point separately (Fig. S2). In contrast to traditional FDM-filaments that often require heating of the build plate, it is paramount to accelerate the gelation process by cooling the print to keep the shape of the extruded biogel stable. This is realized by attaching a commercially available air conditioning system to the printing chamber, which reduces the chamber temperature to about 10-15°C. Therefore, the printed biogel ink is cooled fast enough to keep the gelation time within a few seconds (< 10 s) to allow dimensionally stable printing of complex 3D-objects (Fig. 2 B-D and Movie S1) with aspect ratios over 3 (at a base diameter of 16.6 mm) out of soft biogels with low Young's moduli (< 1 MPa). The width of a single printed line is about 0.6 mm, which results from the nozzle diameter (0.4 mm), the gels viscosity, and the cooling during printing. Consequently, the minimum line spacing where adjacent lines are still separated is 0.5 mm (Fig. 2 E). Notably, the direction of the infill printing lines has negligible influence on the material properties, indicating that there is no preferential polymer orientation induced due to the extrusion process (Fig. S3).

The thermoreversibility of the biogel allows direct reuse in subsequent printing processes. Damaged or obsolete biogel devices are therefore easily recycled by reheating the material and printing new ones (Fig. 2 F). We studied the influence of material storage time, reuse-cycles, and heating time to gain insights into the evolution of the mechanical properties during fabrication. Directly after printing, samples were soft (Young's modulus of 0.27 MPa) and stretchable to about 507% ultimate strain (Fig. 2 G), but subsequently underwent aging and became stiffer with slight changes in stretchability. The ultimate strain changes to 470% after 24 h, which still considerably exceeds the performance of mold-cast biogels by about 140% (Fig. S4). Under storage in ambient conditions, a small fraction of the gel's free water content evaporates, leading to a moderate 10% weight loss within 5 days (Fig. S5 A). At this point. an equilibrium is reached where weight and mechanical properties have stabilized. This stabilization process causes an increase in Young's modulus to 2.2 MPa (Fig. 2 H). The biogel remains stretchable to above 430% ultimate strain and endures an ultimate stress of about 2.2 MPa after 12 days of storage under ambient conditions. We note that the dehydration-induced stiffening of the gel may affect the mechanical response time and, in the case of pneumatic actuators, necessitates higher pressures for the same state of actuation. Generally, soft robotic applications often require Young's moduli in the range of 0.1 to 10 MPa and ultimate strains greater than 200%(*6*); performance metrics that our 3D printed biogels perfectly meet or exceed even after aging.

At the end of a printed part's lifetime, it can be introduced into a reuse cycle that utilizes the biogel's thermoreversibility. We reprinted samples several times to investigate the influence of subsequent prints on the biogels mechanical properties (Fig. 2 I). This procedure leads to an increased Young's modulus after five printing cycles (Fig. S5 B), whereas ultimate strain and ultimate stress remain at 85% and 72%, respectively, of their initial values. After that, further prints failed due to discontinuous extrusion since the biogel became too viscous. Another process that alters the biogels mechanical properties is the temperature-induced degradation of gelatin, which occurs at prolonged heating durations(*26*). In this respect, the required heating time and temperature of the printing process affect its mechanical properties and thus the maximum achievable printing cycles (Fig. 2 J and Fig. S5 C).

When comparing the printed biogels to mold-cast ones, we found that printing yields samples with improved performance, reaching higher stretchability and ultimate stress (Fig. S4). The printed material generally shows a nearly linear stress-strain behavior when stretched to 100% strain and moderate hysteresis under cyclic loading (Fig. 2 K). After the first cycle, where the material is conditioned due to a degree of plastic deformation, the dissipated energy decreases and plateaus at around 13 kJ m^{-3} (Fig. S6). Printing of the biogel can also be used for future designs that benefit from heterogeneous material combinations. Therefore, we studied the adhesion properties of the biogel to various surfaces, including metals, plastic, and wood. The measured debonding energies range from 12.5 J m^{-2} for aluminum up to 220 J m^{-2} for wood (Fig. 2 L and Fig. S7) and are higher than cast gels(*10*).

Printed stretchable waveguide sensors

With the growing demand in device functionality, soft robots require solutions for proprio- and exteroception to allow controlled navigation and interaction with their environment. Networks of stretchable waveguides present an economical choice to implement spatially-resolved sensing for both touch and body deformations(*27*). In particular, lossy waveguides (either with or without cladding) show high sensitivity to length changes when stretched. They can be realized from various materials such as silicone elastomers, ultraviolet (UV) curable resins or hydrogels(*28–31*). Gelatin-based materials benefit from their thermoplastic

properties, which permit large-scale fabrication of waveguides through melt-extrusion(*17*) or, as demonstrated here, rapid and versatile production through 3D-printing.

We printed waveguides without cladding directly from our biogel ink to transmit light utilizing a length-dependent loss to sense deformations (Fig. 3 A). As biogel inks with low sugar to glycerol weight fractions (< 0.35) are highly transparent in the visible and near-infrared (IR) spectrum, the absorption in this region is increased at higher weight fractions (Fig. S8). For strain sensors, the loss mechanisms have to be tuned according to the design, fabrication and quality of the waveguides. When scattering is the dominant mechanism, the material requires high transmittance to allow enough light to be transmitted to the read-out electronics. Besides determining transmittance, the components of the biogel also influence the materials refractive index. We investigated their effects and found that the compound index is a linear combination of the indices of each component weighted by the mass fraction (Fig. S9 and Table S1). This relation is generally valid when each material's refractive index is smaller than 2 and, hence, linearly depends on the material density (see Supplementary Discussion). Tuning the refractive index is of importance for applications that benefit from waveguides with claddings, resulting in step-index fibers. Using hydrogels conveniently allows tuning of the refractive index by adjusting the hydrogel's water content. Yet, the operation of these waveguides in ambient conditions poses a challenge as the evaporation of water increases the refractive index over time. We addressed this issue by substituting some of the biogel's water content with glycerol (Fig. 3B), which increases the bound water content and slows down dehydration(*32*). As a glycerol to water mass ratio (m_{gly}:m_w) of 5:8 leads to a refractive index increase from 1.445 to 1.49 within 10 h, a ratio of 11:2 stabilizes the optical properties at a refractive index of about 1.48. This behavior is quantitatively described by modeling the diffusion kinetics of the water in the biogel (see Supplementary Discussion). However, substituting water with glycerol increases the viscosity of the biogel ink, which negatively influences printability. We found that a glycerol-water mass ratio of 9:4 is a suitable compromise between drying-induced changes and printability and used this composition for our waveguides.

The slab waveguides were printed with a square cross section (2 mm x 2 mm) in a one-step process and connected to light-emitting diodes (LEDs) and photodiodes (PDs) to complete the sensors. The viscosity and surface tension of the melted biogel ink allows printing of generally smooth surfaces, yet the layer morphology—typical for FDM prints—remains visible at the side walls. When stretched, the waveguides show a near linear intensity decrease when extended to 20% or 40% strain and no hysteresis (Fig. 3C, D). The light attenuation here stems from an increased optical path length and hence higher losses through light scattering and absorption. Bending of the waveguides changes the curvature and leads to losses through out-coupling of light, which misses the criteria for total internal reflection. We utilized this mechanism to measure the light intensity as a function of the bending radius, which resulted in an intensity drop of 30% upon a radius change from 72.5 mm to 36 mm (Fig. 3E, F, Fig. S10 and Movie S2).

Additionally, our waveguides function as touch sensors, when they are in contact with external objects or other waveguides. Compressing a region along the waveguide leads to a decrease in transmitted intensity, as light is absorbed or scattered at the newly created interface. Hence, a crossing of two waveguide sensors can be used to localize a touch event on that crossing as the intensity drops in both waveguides. We used this effect to build a video game-style controller pad with six buttons, uniquely resolved by a simple network of three waveguides (Fig. 3 G). The six controller buttons compress the waveguide network at different positions when touched, either at a single waveguide or a crossing of two overlapping waveguides. In this manner, pressing a single button corresponds to a distinct

intensity pattern recorded from the waveguide sensors (Fig. 3 H) and allows to resolve for the button pressed (left, right, up, down, A, B). We used low-cost LEDs and PDs to reduce background noise from ambient light, which operate in the infrared spectrum. Since the infrared background is negligibly small compared to the transmitted light intensity, this leads to a high signal-to-noise ratio and the transmitted intensity is then read out using a current amplifying circuit (Fig. S11).

3D-printed omnidirectional actuators

Soft robotic devices, with their compliance and adaptability, show great potential to improve quality of life, enhance efficiency in industrial processes or enable diverse applications harnessing biomimicry. So far, soft fluidic actuators have been demonstrated in various applications spanning surgical tools(*33*), rehabilitation devices(*34*), grippers(*35*), walking(*36*) and swimming robots(*37*, *38*). The motility of these devices, driven by hydraulic or pneumatic pressure, is guided either by the design of inflatable cavities(*39*) or by reinforcements for movement restriction(*40*, *41*). Single chamber actuators usually only achieve a single DOF movement such as elongation, contraction, bending, or twisting. Applications with higher DOF are realized by combining several modules based on such actuators(*42*) or implementing arrays of inflatable cavities inside their soft bodies(*43*, *44*). Utilizing our 3D-printing technique, we printed a biodegradable pneumatically-driven 3-chamber actuator (16.6 mm diameter, 60 mm height) (Fig. 4 A, S12 A and Movie S3). The parallel arrangement of individually inflatable cavities allows omnidirectional actuation with a single pressure source and three electro-pneumatic pressure regulators. However, this type of actuator experiences a performance loss due to unwanted radial expansion besides the desired longitudinal expansion. Therefore, we applied a cotton fiber reinforcement, which consists mainly of abundant cellulose biopolymers, on the outer walls to increase its bending performance (Fig. S12 B). Adapted to the symmetry of the actuator, three pairs of cotton threads were fixed on its bottom in 120° rotation, alongside the chamber walls. Then one thread of each pair was obliquely wound to the top in a 10° angle clockwise, the other threads counterclockwise. To quantitatively describe the performance of this device, we measured the response time, where the actuator deformation is evaluated following a pressure step. The response times are fast and within 0.63 s at 50 kPa applied pressure (Fig. 4 B). Furthermore, we achieved highly uniform bending performance of individually actuated chambers (Fig. 4 C), which is crucial for reliable positioning and repeatability. Although dehydration of the biogel changes its mechanical properties, we found that the associated increase of response time slows down drastically 24 hours after the fabrication process (Fig. S12 C and D), accounting for reliable controls. Additionally, accurate navigation of these soft devices is challenging due to the non-linear mechanical behavior of the hydrogel, which necessitates the implementation of customized control mechanisms. By capturing and tracking the actuators motion, we created a 2-dimensional map of actuation states and corresponding pressure values (Fig. S12 E and Movie S4). This allowed us to precisely pilot the device to certain positions in real-time and perform predefined motion patterns, using a commercially available videogame controller (Movie S5) or our waveguide sensor controller pad (Movie S6). Despite their ease of control, future applications demand the capability of self-sensing as well as reacting and interacting with their environment. Combining our 3D-printed waveguide sensors with the actuator enables sensing of the bending direction and touch, yet remaining fully biodegradable. We arranged three waveguides alongside each chamber, overlapping at the top, to facilitate the detection of bending in all directions. In this manner, pressurizing a chamber leads to an intensity drop in the corresponding waveguide (Fig. 4 D and Movie S7), which renders the soft robot

exteroceptive even after at least 20 days of aging under ambient conditions (Fig. S13). Furthermore, the design without cladding accounts for higher sensitivity when detecting low-force touch events (Fig. 4 E and Movie S8). The initial contact between the core and any object with higher refractive index than air causes a local change of the angle of total reflection at the respective area. This allows more light to escape, which consequently leads to an intensity drop in addition to losses from mechanical deformation upon applying higher forces.

By combining the features introduced in this work, we implemented a search and wipe routine to remove obstacles in the proximity of the actuator (Fig. 5 and Movie S9). The routine starts with the actuator's tip following a circular path around its center. After this initial calibration, where the respective intensity changes are recorded, the actuator is ready to search for obstacles in its vicinity. On the circular search path our program looks for deviations from the initially recorded intensity values. In this manner the actuator senses contact events with obstacles within its path. Upon detection, the search routine stops and pressure is released from all chambers. Finally, actuation is performed with maximum pressure into the direction of the detected obstacle, which is subsequently pushed away. After the actuator has fulfilled its designated purpose and is no longer of use, it can be disposed of. Immersing it in water triggers the swelling and dissolution of the biogel (Movie S10) and, in the presence of enzymes, complete decomposition. The undissolved parts (e.g. air inlet tubes or cotton threads) can thus be simply taken out and reused or disposed of separately. Alternatively, the coated biogel can readily be recycled after removal of the additional components to create a new generation of sustainable devices (Fig. S14).

DISCUSSION

In this work, we present an omnidirectional soft actuator, 3D-printed from sustainable biomaterials, which features multifaceted sensing capabilities realized by 3D-printed soft optical waveguides. The versatile and high-precision sensor network is capable of acquiring information on the actuators bending state and touch events with objects in its surrounding. This enables the implementation of a search and wipe routine, which allows the soft robot to autonomously localize obstacles in its vicinity and remove them with a push.

Despite the successful implementation of this task, we note that the signal output of the waveguides can vary for similar events. The spatial resolution of touch events alongside the actuator body is difficult, even more so when multiple events occur simultaneously. Therefore, depending on the field of operation, distinguishing between different stimuli (e.g. bending and touching) remains challenging. Implementing distributed fiber-optic networks that operate at various wavelengths or light modulation can help to overcome these limitations(*27*). Interpreting a multitude of signals will be aided by machine learning algorithms to better distinguish multiple deformations(*45*) and thus enhance the versatility of this robot design.

Increasing the level of complexity will also require more advanced actuator shapes and multi-material combinations. So far, the viscosity and cooling time hinder printing of overhanging features or cavities. Developing suitable biodegradable support materials will solve these issues in combination with multi-material printing. Moreover, multi-material printing will enable combinations of mechanically, electrically, and optically tuned biogels to achieve actuation mechanisms beyond pneumatic control and enhance sensing and control capabilities for highly integrated robots.

Accompanying technical improvements, end-of-life considerations are critical for future sustainable development. The main structure of our robot, including the fiber reinforcement and waveguides, is entirely biodegradable. Additionally, the biogel's water solubility enables a simple method to separate the robot from its non-biodegradable control parts, allowing their reuse. Alongside this eco-friendly fabrication approach using biodegradable materials, we introduced an additional reuse cycle where the biogel is reprinted up to 5 times, maintaining more than 70% of the initial performance metrics. More reprint cycles could be realized by restoring the printability through rehydration of the biogel and reducing the printing temperature or shortening the heating period by increasing the printing speed. The presented accessible, sustainable and cost-effective fabrication strategy will likely have a positive influence on soft and collaborative robotics through a reduced ecological footprint.

MATERIALS AND METHODS

Materials

The biogel inks are based on previously reported recipes(*10*). Sugar syrup (7 g) was heated to 60°C to reduce its viscosity. Citric acid (1 g) and glycerol (9 g) were dissolved in deionized (DI) water (4 g), added to the syrup, and stirred until it formed a homogeneous mixture. Then gelatin powder (6.66 g) was added and allowed to soak for at least 24 h. The mixture was then heated in an oven at 85°C for 1 h 15 min and mixed in a planetary mixer (DAC 600.2 VAC-P, Hauschild Engineering) under vacuum (2,350 rpm., 350 mbar) for 3.5 min to get a homogeneous solution, which was then filled in 10 mL syringes. Variations of used biogel compositions are listed in Table S3.
The shellac-polyethylene glycol (PEG) solution was prepared according to Luangtana-Anan et al.(*46*). Shellac flakes (6 g) were dissolved in ethanol (10 g) under continuous stirring. Polyethylene glycol (0.6 g) was then mixed into the solution and stirred until homogeneously distributed.

Printing of biogel inks

The biogel ink was printed with a reservoir temperature of 75°C and a nozzle temperature of 65°C. The printing speed depends on the geometry of the print since it is defined by a 'minimum time per layer' value which was set 90 s and a maximum speed of 1000 mm min^{-1}. The layer height was set to 0.2 mm.

All samples for tensile testing were printed under ambient conditions without additional cooling. For all other prints additional cooling was used to ensure dimensionally stable printing of 3D objects.

For the printing angle test, several samples series were prepared, where the printing direction of subsequent layers is shifted by an angle α (Fig. S3 A) and tensile tests were conducted for varying α between 0° and 180° (Fig. S3 B).

For the resolution test, a single-lined meander structure with decreasing line spacing was printed. Starting with a gap of 10 mm, the line spacing was reduced by 1 mm each step. After reaching 1 mm, it was halved for two steps down to 0.25 mm.

Mechanical characterization

Standardized dumbbell-shaped samples (ISO527-2:1996(5A)) were prepared for uniaxial tensile tests. All tests were performed at ambient conditions on a uniaxial tensiometer (Zwick Roell Z005, 100 N load cell) at a strain rate of 50 mm min^{-1}. Young's modulus was obtained using a modified hyperelasticity model for neo-Hookean solids (see Supplementary Discussion).

For the drying experiments the samples were stored under ambient conditions. The stated sample age is the storage time after printing.

For the recycling and heating duration experiments, the samples were stored in a climate chamber at 23°C and 50% relative humidity (rH). Testing was then done 24 h after each print if not stated otherwise.

For the recycling of shellac coated biogels, the samples were coated with the shellac-PEG solution after printing and stored for 24 h under ambient conditions. The combined material was then recycled and again samples were printed and stored for 24 h under ambient conditions before testing.

Cyclic tensile tests were performed for 8 cycles and 100% strain. The samples were printed and stored for 24 h under ambient conditions beforehand. Energy dissipation was then calculated from the area between extension and relaxation curve.

For adhesion tests, biogels (120 mm x 30 mm x 2 mm) were printed directly on different substrates on an area of 70 mm x 30 mm and the excess end of 50 mm x 30 mm was printed on Polyethylene terephtalat (PET) foil. A sheet of the same PET foil was put on top of the samples and they were stored for 24 h under ambient conditions. The foils were applied to prevent elongation of the biogel samples during peel tests. The excess end of the biogel was then fixed in the tensiometer at an angle of 90° and the biogel was peeled off of the substrate at a rate of 50 mm min^{-1}. The debond energy was then calculated from the seperating force (see Supplementary Discussion).

For a comparison of printing to mold-casting, three different preparation methods were tested. Mold-casting of a sheet and punching out test samples are called method A (Fig. S4 A), 3D-printing of a sheet and punching out test samples method B (Fig. S4 B) and entirely printed test samples method C (Fig. S4 C). The cast samples were sealed airtight for 48 h after casting and dried under ambient conditions for another 24 h, whereas the printed samples were dried for 72 h before they were tested.

Optical characterization

Molten biogel was cast into a mold, to form a sheet of the desired thickness, where it cooled down for at least 48 hours. Then the samples were cut out of the sheet.

To determine the refractive index, 1 mm thick samples were measured with an analog Abbe-refractometer (AR4, Kruess Optronics GmbH) at a wavelength of λ = 589 nm. The temperature of the illumination and measuring prism was kept between 18-22.5°C using water-cooling (TC9, Tamson).

A set of refractive index measurements was performed with different constituents' masses. Each set of experiments is listed in Table S3.

2 mm thick samples were prepared, and experiments were conducted 12 h after casting to measure the change in refractive index over time. The samples were suspended to dry atmosphere (23°C, 40% rH) for 10 h. Once per hour, the samples were taken out of the chamber to measure the refractive index. The temperature of the refractometer's illumination and measuring prism remained between 23.4 and 26.4°C.

The absorbance of biogel compounds was measured using a spectrophotometer (LAMBDA 1050 UV/Vis Spectrophotometer, PerkinElmer). The biogel was cast into a 10 mm x 10 mm flask made of quartz glass (OS High Precision Cell, Hellma Analytics) and measured alongside a reference sample containing distilled water (18 kΩ) over a spectrum of 250-800 nm.

Waveguides and waveguide-controller

The waveguides in this work are slab waveguides without cladding, with a cross section of 2 mm x 2 mm. They are entirely 3D-printed of the biogel ink.

We used LEDs and PDs with spectral range in the infrared (LED: Osram SFH4350, PD: Osram SFH229FA) to lower background noise from ambient light. They were coupled to the waveguides by melting the waveguides' ends locally and pressing them onto the tips of the LEDs and PDs. For intensity readouts, we used an Arduino Nano (Arduino s.r.l.). The LEDs were driven by the Arduinos digital ports and the PDs were read out on its analog ports by using simple amplification circuits (Fig. S11).

The test setup for bending measurements is based on a commercially available 3D-printer (Fig. S10). A piece of PET filament of 2.85 mm diameter was fixed on one end and rotatably mounted on the printer's x-axis. In this way, the filament forms a circular shape and its diameter can be adjusted by moving the x-axis carriage of the printer. The waveguide was fixed to the filament to follow the diameter changes as intensity readouts were performed.

For the waveguide controller, the waveguides were placed in a specially designed network, embedded in the waveguide pad, as sketched in Fig. 3 G. To avoid crosstalk between the waveguides, the waveguide pad was printed of an IR absorbing terracotta composite filament and the side faces of the LEDs were coated with several layers of black spray paint. The electronics, including the Arduino Nano were embedded into the controller housing.

Fabrication and control of pneumatic actuators

The main body is cylindrical with three chambers inside, arranged in 120° rotation. It has a total height of 6.5 cm with a wall thickness of 2 mm and 5 mm top and bottom thickness. Improved bending movement is achieved by utilizing fiber reinforcement to prevent radial expansion. This reinforcement consists of cotton threads obliquely wound around the biogel cylinder.

The fabrication starts with a semi-closed 3-chambered cylinder, which was 3D-printed on top of six cotton threads that were arranged pairwise in 120° rotation on the building plate. Afterwards, one thread of each pair was wound around the cylinder at an angle of 10° to the top in a clockwise manner, the other three threads counterclockwise. The threads were then fixed onto the cylinder's surface by applying a thin layer of shellac-PEG solution, which formed a flexible coating after evaporation of the solvent. Silicone tubes (outer diameter 1.65 mm, inner diameter 0.76 mm; Freudenberg Medical) of 10 cm length were dip-coated on one end (1 cm) with the actuator end-cap gel (Table S3) and inserted into a preheated mold (60°C) of cylindrical shape (18 mm diameter, 8 mm height). The same biogel, heated up to 95°C, was then poured into the mold, followed by partial insertion of the semi-open cylinder into the biogel to close the actuator. The actuator was released from the mold after the biogel was cooled down and polymerized.

For tracking and mapping the pressure, a red ball (10 mm diameter) was attached to the actuator's top. The actuator's chambers were then pressurized and movement was recorded

on video from a top view of the setup. Pressures, ranging from 0 to 46 kPa, were applied in 2 kPa steps to 2 chambers at a time in all possible combinations. The path of the colorized ball was tracked using image processing features of the OpenCV libraries and the final coordinates for each pressure combination were determined. These coordinates were then normalized to a radius of 1 and mapped to corresponding pressure values. This resulted in a 2D pressure-map of individually addressable positions.

Actuation was controlled by three pneumatic valves (ITV 0030-3BS, SMC) which control the pressure of the individual chambers proportionally to their input signals. These input signals were controlled using a microcomputer (Raspberry Pi, Raspberry Pi Foundation). Actuation was achieved either directly, via lists of pressure values and corresponding coordinates, or dynamically. Dynamic controls were implemented by using a commercially available joystick controller (Dualshock 4 Wireless-Controller, Sony Corporation). Coordinates of the joystick's position were compared to the entries of the 2D pressure-map in real-time. Signals proportional to the pressure values of the entry with the smallest distance were then sent to the valves.

Actuator characterization

Experiments were conducted in controlled environmental conditions using a climate chamber (23°C, 40% rH) 24 h after fabrication of the actuator, unless otherwise stated. A red stick (3 mm diameter, 15 mm length) was mounted on the actuator's top to allow reliable tracking of its movement. A single chamber was pressurized, and the movement was recorded on video from a perspective perpendicular to the actuator's plane of movement. Bending angles were then calculated as the enclosing angle of the actuator's top plane's normal in a relaxed and pressurized state. The plane's normal corresponds to the red stick's position, determined using image processing features of Mathematica. Measurements were repeated 5 times and values are presented using the mean value and the standard deviation, respectively.

Bending performance was analyzed for each of the three chambers of one actuator. Pressure values ranged from 0 kPa to 60 kPa with steps of 2.5 kPa. The maximum bending angle was determined by pressurizing one chamber until failure. Pressure values started at 0 kPa with steps of 2.5 kPa. Bending angles were determined for the fully pressurized state directly before relaxation.

The actuator's response with step-wise applied pressure was conducted on a single chamber of one actuator. A pressure of 50 kPa was applied for two seconds, with the recording started before and stopped after in the same intervals. Bending angles were determined for every frame of the video (60 fps). The time in which the actuator reaches 90% of the final bending angle was determined as an indicator of performance named response time. Step response experiments were repeated every 30 minutes for 70.5 h with a pressure of 40 kPa, starting right after the fabrication process was finished. The indicator of performance was again the time when the actuator reached 90% of its final bending angle (Fig. S12 C).

For the dissolution experiment, a 3-chamber actuator was put into a glass beaker, filled with 150 mL DI water and left in a climate chamber at 23°C and 50% rH for 40 h.

To analyze aging, an actuator was prepared and assembled with waveguide sensors. Actuation was performed after 20 days supplying 90 kPa pressure. The intensity readings from the waveguide sensors were recorded simultaneously.

Statistics

Each data point represents a mean value of n samples as indicated in the corresponding figure captions. Error bars and error bands represent the standard deviation.

Supplementary Materials

Fig. S1. Biodegradation of biogels via biochemical oxygen demand (BOD).
Fig. S2. Biogel extruder with integrated heating system.
Fig. S3. Mechanical properties for different printing patterns.
Fig. S4. Comparison of preparation methods.
Fig. S5. Weight loss and Young's modulus change of printed biogel samples over time.
Fig. S6. Energy dissipation of printed biogel for 8 consecutive loading cylces.
Fig. S7. Peel tests of biogel directly printed onto different substrates.
Fig. S8. Transmittance measurements for gelatin biogels with different weight fractions of glucose and glycerol.
Fig. S9. Refractive index of gelatin-based biogel depending on the concentration of its constituents.
Fig. S10. Experiment setup for waveguide bending measurements.
Fig. S11. Schematic of the amplification circuit for photodiode readout.
Fig. S12. 3-chamber soft gelatin actuator.
Fig. S13. Actuation of a 20 days old actuator assembled with waveguide sensors.
Fig. S14. Recycling of printed biogel samples with shellac coating.

Table S1. Reference refractive indices of the biogel ingredients in this work.
Table S2. Characteristic decaying constants.
Table S3. List of the weight in grams of all materials involved in fabricating the gelatin-based hydrogel compounds in this work.

Movie S1. Biogel printing of a calibration cube.
Movie S2. Waveguide bending.
Movie S3. Biogel printing of an actuator.
Movie S4. Position tracking of actuation states.
Movie S5. Interactive actuator piloting.
Movie S6. Piloting actuator with waveguide controller.
Movie S7. Actuator sensing bending motion.
Movie S8. Actuator sensing finger touch.
Movie S9. Search and wipe routine.
Movie S10. Actuator dissolution in water.

References only cited in Supplementary Materials:
(*47*, *48, 49*)

References

1. G.-Z. Yang, J. Bellingham, P. E. Dupont, P. Fischer, L. Floridi, R. Full, N. Jacobstein, V. Kumar, M. Mcnutt, R. Merrifield, B. J. Nelson, B. Scassellati, M. Taddeo, R. Taylor, M. Veloso, Z. L. Wang, R. Wood, The grand challenges of Science Robotics. *Sci. Robot.* **3**, 31 (2018).

2. M. Cianchetti, C. Laschi, A. Menciassi, P. Dario, Biomedical applications of soft robotics. *Nat. Rev. Mater. 2018 36*. **3**, 143–153 (2018).
3. J. Yin, R. Hinchet, H. Shea, C. Majidi, J. Yin, C. Majidi, R. Hinchet, H. Shea, Wearable Soft Technologies for Haptic Sensing and Feedback. *Adv. Funct. Mater.* **31**, 2007428 (2021).
4. G. M. Whitesides, Soft Robotics. *Angew. Chemie Int. Ed.* **57**, 4258–4273 (2018).
5. V. Forti, C. P. Balde, R. Kuehr, G. Bel, The Global E-waste Monitor 2020: Quantities, flows and the circular economy potential. *United Nations Univ. (UNU)/United Nations Inst. Train. Res. – co-hosted SCYCLE Program. Int. Telecommun. Union Int. Solid Waste Assoc. (ISWA), Bonn/Geneva/Rotterdam*, 1–119 (2020).
6. F. Hartmann, M. Baumgartner, M. Kaltenbrunner, Becoming Sustainable, The New Frontier in Soft Robotics. *Adv. Mater.* **33**, 2004413 (2021).
7. S. Walker, J. Rueben, T. Van Volkenburg, S. Hemleben, C. Grimm, J. Simonsen, Y. Mengüç, Using an environmentally benign and degradable elastomer in soft robotics. *Int. J. Intell. Robot. Appl.* **1**, 124–142 (2017).
8. A. Pena-Francesch, H. Jung, M. C. Demirel, M. Sitti, Biosynthetic self-healing materials for soft machines. *Nat. Mater.* **19**, 1230–1235 (2020).
9. J. Shintake, H. Sonar, E. Piskarev, J. Paik, D. Floreano, Soft pneumatic gelatin actuator for edible robotics. *IEEE Int. Conf. Intell. Robot. Syst.* **2017**-**Septe**, 6221–6226 (2017).
10. M. Baumgartner, F. Hartmann, M. Drack, D. Preninger, D. Wirthl, R. Gerstmayr, L. Lehner, G. Mao, R. Pruckner, S. Demchyshyn, L. Reiter, M. Strobel, T. Stockinger, D. Schiller, S. Kimeswenger, F. Greibich, G. Buchberger, E. Bradt, S. Hild, S. Bauer, M. Kaltenbrunner, Resilient yet entirely degradable gelatin-based biogels for soft robots and electronics. *Nat. Mater.* **19**, 1102–1109 (2020).
11. V. H. M. Mouser, F. P. W. Melchels, J. Visser, W. J. A. Dhert, D. Gawlitta, J. Malda, Yield stress determines bioprintability of hydrogels based on gelatin-methacryloyl and gellan gum for cartilage bioprinting. *Biofabrication* **8**, 35003 (2016).
12. F. Gao, Z. Xu, Q. Liang, H. Li, L. Peng, M. Wu, X. Zhao, X. Cui, C. Ruan, W. Liu, Osteochondral Regeneration with 3D-Printed Biodegradable High-Strength Supramolecular Polymer Reinforced-Gelatin Hydrogel Scaffolds. *Adv. Sci.* **6**, 1900867 (2019).
13. T. Pan, W. Song, X. Cao, Y. Wang, 3D Bioplotting of Gelatin/Alginate Scaffolds for Tissue Engineering: Influence of Crosslinking Degree and Pore Architecture on Physicochemical Properties. *J. Mater. Sci. Technol.* **32**, 889–900 (2016).
14. F. You, X. Wu, X. Chen, 3D printing of porous alginate/gelatin hydrogel scaffolds and their mechanical property characterization. *Int. J. Polym. Mater. Polym. Biomater.* **66**, 299–306 (2017).
15. A. Tijore, S. A. Irvine, U. Sarig, P. Mhaisalkar, V. Baisane, S. Venkatraman, Contact guidance for cardiac tissue engineering using 3D bioprinted gelatin patterned hydrogel. *Biofabrication* **10**, 025003 (2018).
16. H. Ceylan, I. C. Yasa, O. Yasa, A. F. Tabak, J. Giltinan, M. Sitti, 3D-Printed Biodegradable Microswimmer for Theranostic Cargo Delivery and Release. *ACS Nano*. **13**, 3353–3362 (2019).
17. F. Sordo, E. R. Janecek, Y. Qu, V. Michaud, F. Stellacci, J. Engmann, T. J. Wooster, F. Sorin, Microstructured Fibers for the Production of Food. *Adv. Mater.* **31**, 1807282 (2019).
18. A. Pfister, R. Landers, A. Laib, U. Hübner, R. Schmelzeisen, R. Mülhaupt, Biofunctional Rapid Prototyping for Tissue-Engineering Applications: 3D Bioplotting versus 3D Printing. *J. Polym. Sci. Part A Polym. Chem.* **42**, 624–638 (2004).
19. J. Wang, F. Tang, Y. Wang, Q. Lu, S. Liu, L. Li, Self-Healing and Highly Stretchable Gelatin Hydrogel for Self-Powered Strain Sensor. *ACS Appl. Mater. Interfaces* **12**, 1558–1566 (2020).

20. C. Zhu, R. Yang, X. Hua, H. Chen, J. Xu, R. Wu, L. Cen, Highly stretchable HA/SA hydrogels for tissue engineering. *J. Biomater. Sci. Polym. Ed.* **29**, 543–561 (2018).
21. J. Y. Sun, X. Zhao, W. R. K. Illeperuma, O. Chaudhuri, K. H. Oh, D. J. Mooney, J. J. Vlassak, Z. Suo, Highly stretchable and tough hydrogels. *Nature*. **489**, 133–136 (2012).
22. D. B. K. Lim, H. Gong, Highly stretchable and transparent films based on cellulose. *Carbohydr. Polym.* **201**, 446–453 (2018).
23. R. Tong, G. Chen, D. Pan, H. Qi, R. Li, J. Tian, F. Lu, M. He, Highly Stretchable and Compressible Cellulose Ionic Hydrogels for Flexible Strain Sensors. *Biomacromolecules* **20**, 2096–2104 (2019).
24. R. Rai, M. Tallawi, A. Grigore, A. R. Boccaccini, Synthesis, properties and biomedical applications of poly(glycerol sebacate) (PGS): A review. *Prog. Polym. Sci.* **37**, 1051–1078 (2012).
25. R. Horne, Reprap development and further adventures in DIY 3D printing: Universal Paste extruder - Ceramic, Food and Real Chocolate 3D Printing, (available at https://richrap.blogspot.com/2012/04/universal-paste-extruder-ceramic-food.html).
26. R. Schrieber, H. Gareis, *Gelatine Handbook: Theory and Industrial Practice* (Wiley-VCH, 2007; http://dnb.d-nb.dei.).
27. H. Bai, S. Li, J. Barreiros, Y. Tu, C. R. Pollock, R. F. Shepherd, Stretchable distributed fiber-optic sensors. *Science* **370**, 848–852 (2020).
28. H. Zhao, K. O'Brien, S. Li, R. F. Shepherd, Optoelectronically innervated soft prosthetic hand via stretchable optical waveguides. *Sci. Robot.* **1** (2016), doi:10.1126/scirobotics.aai7529.
29. S. Liu, L. Li, Ultrastretchable and Self-Healing Double-Network Hydrogel for 3D Printing and Strain Sensor. *ACS Appl. Mater. Interfaces* **9**, 26429–26437 (2017).
30. J. B. Chossat, Y. L. Park, R. J. Wood, V. Duchaine, A soft strain sensor based on ionic and metal liquids. *IEEE Sens. J.* **13**, 3405–3414 (2013).
31. X. G. Yu, Y. Q. Li, W. Bin Zhu, P. Huang, T. T. Wang, N. Hu, S. Y. Fu, A wearable strain sensor based on a carbonized nano-sponge/silicone composite for human motion detection. *Nanoscale* **9**, 6680–6685 (2017).
32. S. Sanwlani, P. Kumar, H. B. Bohidar, Hydration of gelatin molecules in glycerol-water solvent and phase diagram of gelatin organogels. *J. Phys. Chem. B*. **115**, 7332–7340 (2011).
33. T. Ranzani, G. Gerboni, M. Cianchetti, A. Menciassi, A bioinspired soft manipulator for minimally invasive surgery. *Bioinspiration and Biomimetics* **10**, 035008 (2015).
34. P. Polygerinos, Z. Wang, K. C. Galloway, R. J. Wood, C. J. Walsh, Soft robotic glove for combined assistance and at-home rehabilitation. *Rob. Auton. Syst.* **73**, 135–143 (2015).
35. J. Shintake, V. Cacucciolo, D. Floreano, H. Shea, Soft Robotic Grippers. *Adv. Mater.* **30**, 1707035 (2018).
36. R. F. Shepherd, F. Ilievski, W. Choi, S. A. Morin, A. A. Stokes, A. D. Mazzeo, X. Chen, M. Wang, G. M. Whitesides, Multigait soft robot. *Proc. Natl. Acad. Sci. U. S. A.* **108**, 20400–20403 (2011).
37. A. D. Marchese, C. D. Onal, D. Rus, Autonomous Soft Robotic Fish Capable of Escape Maneuvers Using Fluidic Elastomer Actuators. *Soft Robot.* **1**, 75–87 (2014).
38. K. Suzumori, S. Endo, T. Kanda, N. Kato, H. Suzuki, A bending pneumatic rubber actuator realizing soft-bodied manta swimming robot. *Proc. - IEEE Int. Conf. Robot. Autom.*, 4975–4980 (2007).
39. B. Mosadegh, P. Polygerinos, C. Keplinger, S. Wennstedt, R. F. Shepherd, U. Gupta, J. Shim, K. Bertoldi, C. J. Walsh, G. M. Whitesides, Pneumatic networks for soft robotics that actuate rapidly. *Adv. Funct. Mater.* **24**, 2163–2170 (2014).
40. P. Polygerinos, Z. Wang, J. T. B. Overvelde, K. C. Galloway, R. J. Wood, K. Bertoldi, C. J. Walsh, Modeling of Soft Fiber-Reinforced Bending Actuators. *IEEE Trans. Robot.* **31**,

778–789 (2015).
41. R. V. Martinez, C. R. Fish, X. Chen, G. M. Whitesides, Elastomeric origami: Programmable paper-elastomer composites as pneumatic actuators. *Adv. Funct. Mater.* **22**, 1376–1384 (2012).
42. F. Connolly, P. Polygerinos, C. J. Walsh, K. Bertoldi, Mechanical programming of soft actuators by varying fiber angle. *Soft Robot.* **2**, 26–32 (2015).
43. K. Suzumori, S. Iikura, H. Tanaka, Flexible microactuator for miniature robots. *Proceedings. IEEE Micro Electro Mech. Syst.*, 204–209 (1991).
44. R. V. Martinez, J. L. Branch, C. R. Fish, L. Jin, R. F. Shepherd, R. M. D. Nunes, Z. Suo, G. M. Whitesides, Robotic tentacles with three-dimensional mobility based on flexible elastomers. *Adv. Mater.* **25**, 205–212 (2013).
45. Z. Ding, N. F. Lepora, E. Johns, Sim-to-Real Transfer for Optical Tactile Sensing. *Proc. - IEEE Int. Conf. Robot. Autom.*, 1639–1645 (2020).
46. M. Luangtana-Anan, J. Nunthanid, S. Limmatvapirat, Effect of molecular weight and concentration of polyethylene glycol on physicochemical properties and stability of shellac film. *J. Agric. Food Chem.* **58**, 12934–12940 (2010).
47. Organisation for Economic Co-operation and Development (OECD), "Test No. 301: Ready Biodegradability" (Publication 9789264070349, OECD, 1992; www.oecd-ilibrary.org/content/publication/9789264070349-en).
48. J. B. Arago D. F. J.; Biot, No Title. *Mém. Acad. Fr.*, 7–9 (1806).
49. Citric acid | C6H8O7 - PubChem, (available at https://pubchem.ncbi.nlm.nih.gov/compound/311).

Acknowledgments:
The authors thank D. Danninger for the support in figure design.

Funding:
European Research Council Starting Grant 'GEL-SYS' under grant agreement no. 757931
Austrian Research Promotion Agency GmbH (FFG) within the COMET-project TextileUX under grant agreement no. 865791

Author contributions:

MK, MB and MD conceived the project; AH and MD developed and characterized the 3D-printer; MB supervised the biogel development ; AH, DP, LL and EW prepared the biogels; AH, MB, EW and RG characterized the printed biogel samples and AH, MB, EW and FH analyzed the data; FH supervised the development of waveguide sensors; LL conducted the optical characterization of the biogel, analyzed the data and developed the theoretical model; AH conducted the characterization of the waveguide sensors and analyzed the data. DP and MB developed and characterized the pneumatic actuator, analyzed the data and developed the control setup and software; AH and DP developed the actuator with integrated waveguides, designed the experiments and AH, DP and DS wrote the software; MK gave input at all stages; AH, DP, LL, FH and MK designed the figures and wrote the manuscript; All authors contributed to editing the manuscript; MK supervised the research.

Competing interests: The authors declare that they have no competing interests.

Data and materials availability: All data needed to evaluate the conclusions in the paper are available in the main text or the supplementary materials.

Figures:

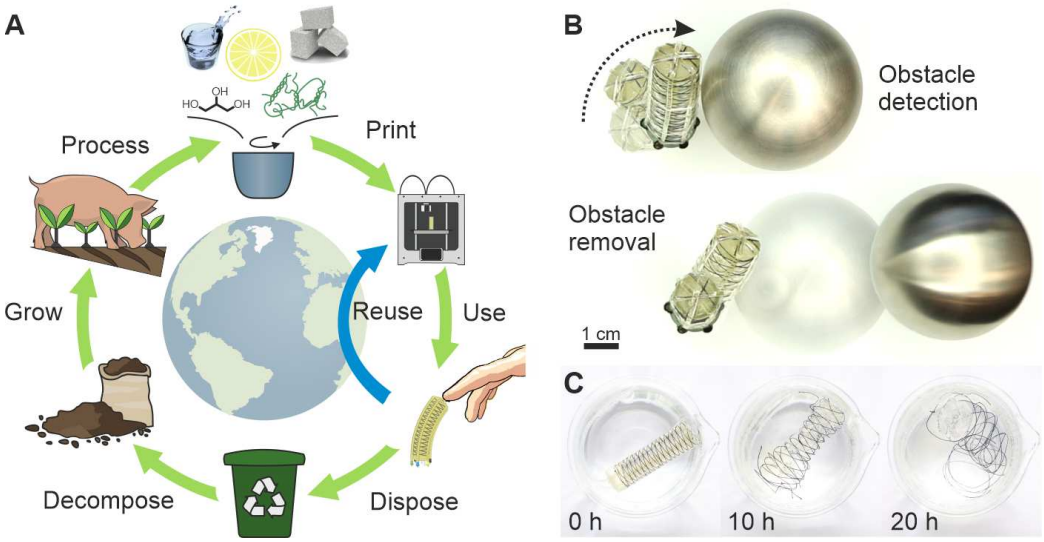

Fig. 1. Sustainable 3D-printed soft actuators with integrated waveguide sensors. (**A**) Biodegradable constituents enable a cradle-to-cradle design for soft robotics, where thermoreversibility opens an additional subcycle for multiple usage and extended lifetime. (**B**) Three-chamber pneumatic actuator with fiber reinforcement and integrated optical sensors. The sensors detect obstacles in the path of the actuator and allow removal of the object. (**C**) When immersed in water, the gelatin actuator and waveguides swell and dissolve. Complete biodegradation is enabled in sewage or compost.

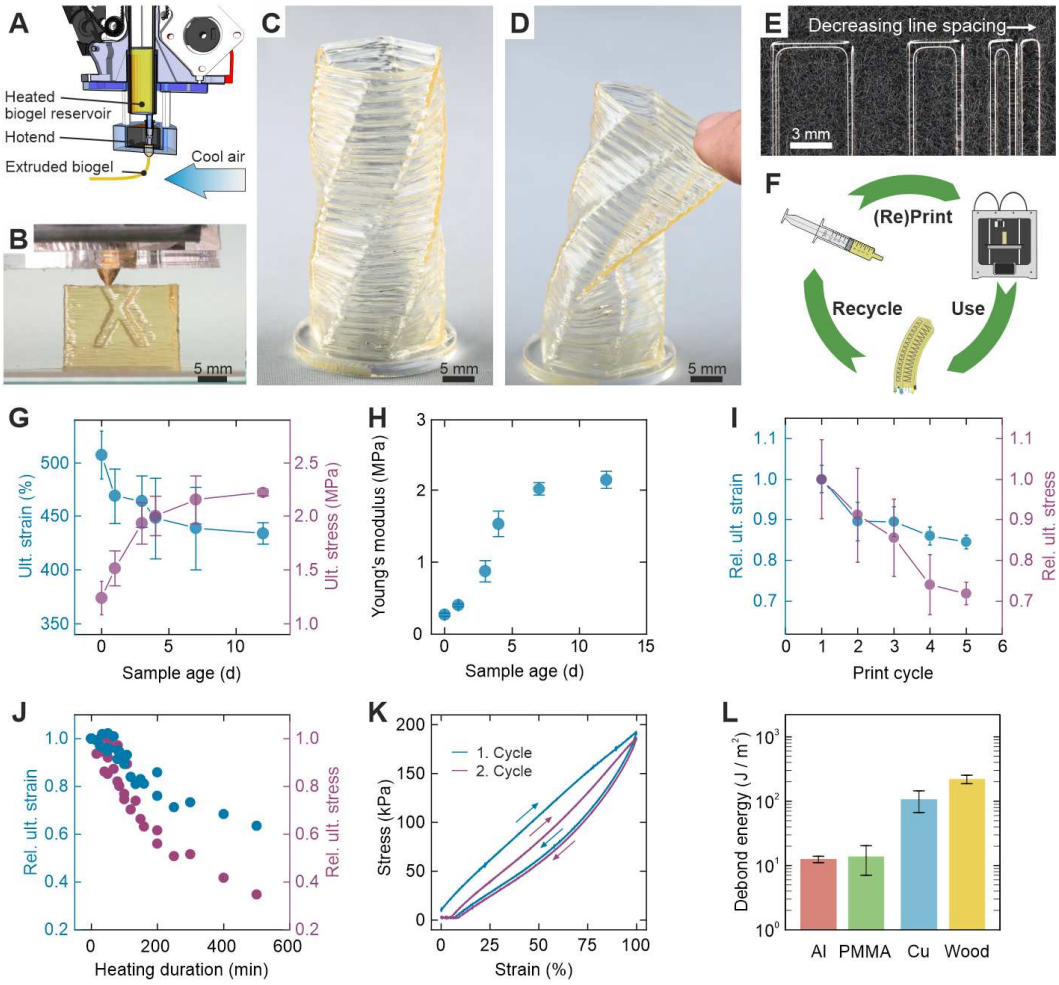

Fig. 2. 3D-printing of gelatin-based biogel. (**A**) Extrusion scheme of the two-stage heating system. Upon extrusion, the gelation is accelerated by a cool airflow. (**B**) Printing of a solid calibration cube. (**C**) Printed twisted vase with a wall thickness of 0.8 mm. (**D**) The soft structure and low Young's modulus allow reversible deformation. (**E**) Resolution test of single lines (~ 0.6 mm width) with decreasing line spacing from left to right, starting at 5 mm. On the right side, lines with 0.5 mm spacing are still separated, whereas a 0.25 mm spacing results in fused lines. (**F**) Printed parts can be recycled by heating and reprinting the material. (**G**) Change of the sample's mechanical properties due to drying under ambient conditions. Error bars: standard deviation for $n \geq 3$ samples. (**H**) Change in Young's modulus with sample age, stored under ambient conditions. Error bars: standard deviation for $n \geq 3$ samples. (**I**) Relative change of mechanical properties due to consecutive recycling cycles. Error bars: standard deviation for $n \geq 3$ samples. (**J**) Relative change of mechanical properties due to gelatin degradation upon continuous heating. (**K**) Hysteresis of biogel samples under 100% strain for the first two cycles. (**L**) Debond energy of biogels directly printed onto different substrates (aluminum, PMMA, copper, wood). Error bars: standard deviation for $n = 3$ samples.

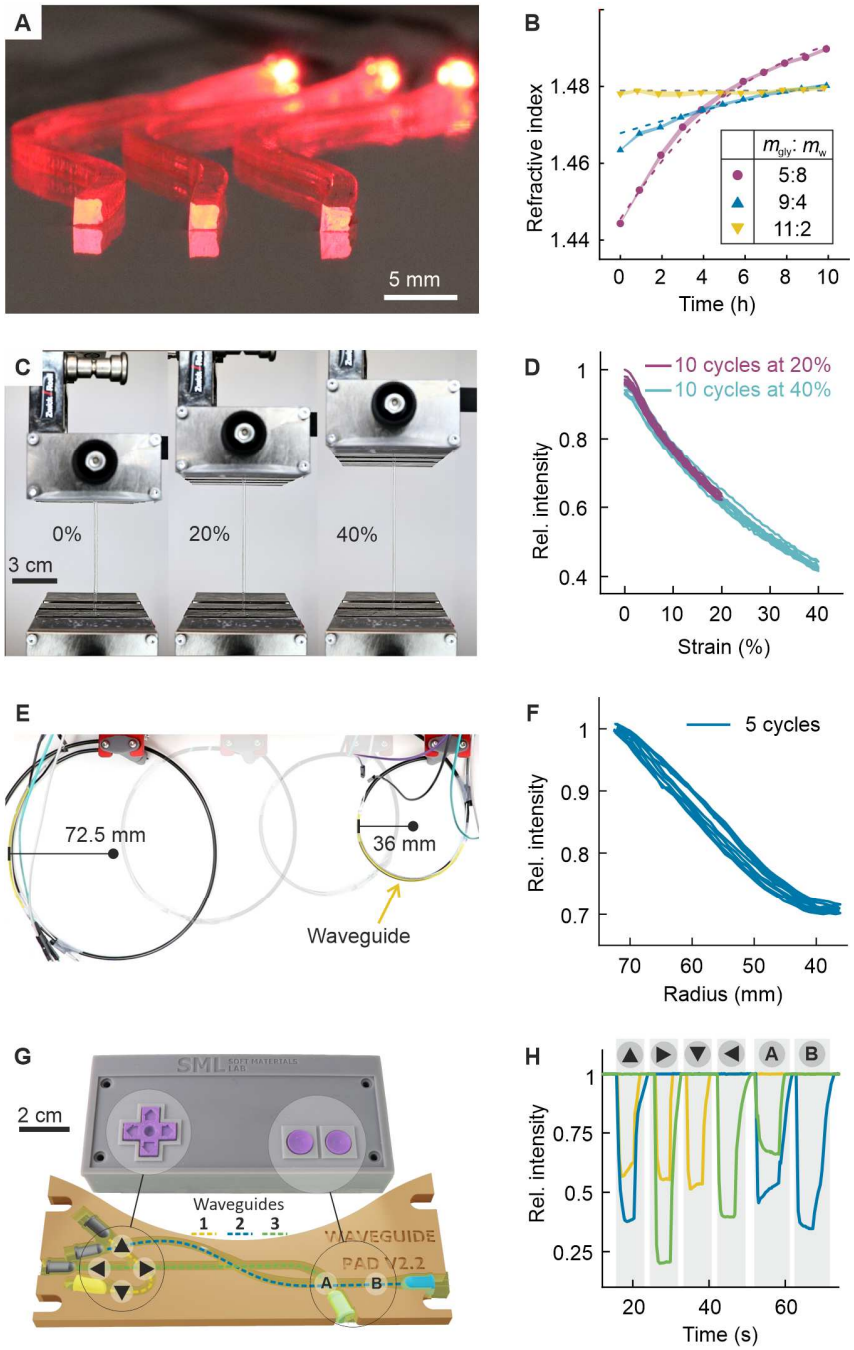

Fig. 3. 3D-printed gelatin-based stretchable waveguides. (**A**) Gelatin waveguides transmit the light of red LEDs. (**B**) Change of refractive index as function of storage time in ambient conditions. Refractive index of high water-content m_w biogels increases due to water evaporation but is suppressed by increasing the glycerol content m_{gly}. The dashed lines represent the theoretical model. The fit parameters can be found in Supplementary Table S2. For the respective constituent compounds, see Supplementary Table S3. Error band: standard deviation for n = 5 samples. (**C**) Waveguides stretch to large deformations above 40% strain. (**D**) Change of transmitted light intensity due to a length change when stretched. Strain response shows no hysteresis throughout 10 consecutive stretch-and-release cycles to 20% strain, followed by 10 cycles to 40% strain. (**E**) Overlay image of the waveguide bending experiment. (**F**) Change of transmitted light intensity shows linear behavior due to a bending radius change. (**G**) Controller pad with touch responsive

waveguides. Three waveguide sensors are arranged to resolve six input buttons. (**H**) Applying pressure on an intersection of two waveguides results in a specific intensity drop, which is characteristic for the pressed button.

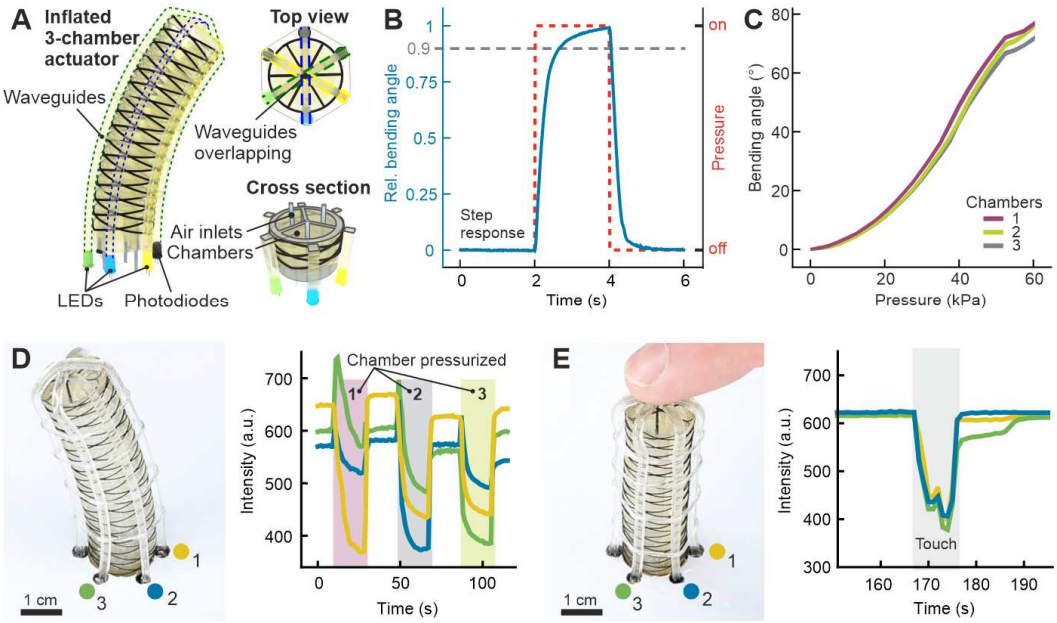

Fig. 4. Performance of multi-directional self-sensing actuators. (**A**) Waveguide sensors are placed over the actuator and cross each other on the top to sense both bending state and touch inputs. (**B**) Step response of the actuator's bending angle upon pressurizing one of the three chambers. 90% of the fully bent state is reached within 0.63 s. (**C**) Bending angle versus pressure characteristics for all three chambers. (**D**) The actuator's bending direction is inferred from the intensity pattern of the waveguides. When a chamber is pressurized, the intensity drops most in the closest waveguide. (**E**) When touching the tip of the actuator (grey area in graph), the intensity on all three waveguides drops.

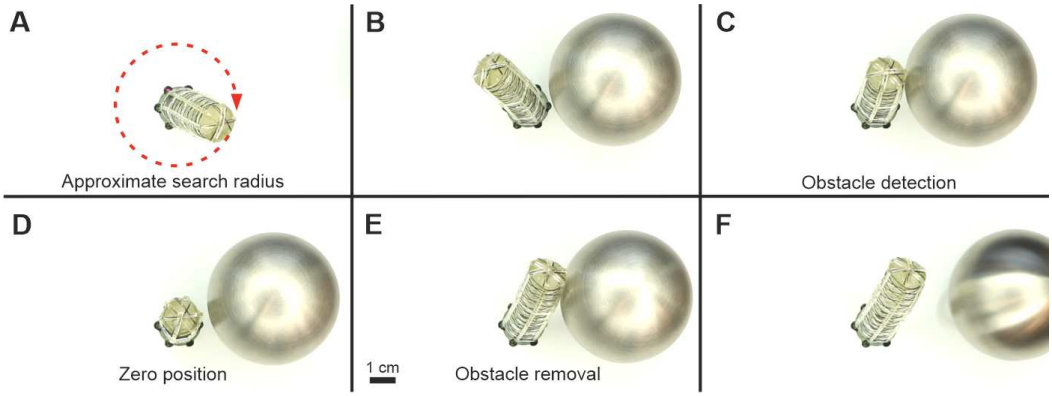

Fig. 5. Search and wipe routine. (**A - C**) The actuator performs a circular motion until it detects an unexpected intensity drop upon hitting an obstacle. (**D - F**) After detection, from its starting position, maximum pressure is applied in the direction of the obstacle to remove it.